

Some Enabling Techniques for Polarization Mode Dispersion Compensation

D. Sandel, V. Mirvoda, S. Bhandare, F. Wüst, and R. Noé, *Member, IEEE*

This material is posted here with permission of the IEEE. Internal or personal use of this material is permitted. However, permission to reprint/republish this material for advertising or promotional purposes or for creating new collective works for resale or redistribution must be obtained from the IEEE by writing to pubs-permissions@ieee.org. By choosing to view this document, you agree to all provisions of the copyright laws protecting it.

Abstract—Progress toward 40-Gb/s polarization-mode dispersion (PMD) compensation is presented in several areas. A single-waveplate polarization scrambler that generates Stokes' parameters with just three harmonics has been realized. Together with an arrival-time detection scheme, it allows the detection of about 1 ps of PMD within 2.4 μ s in a 40-Gb/s nonreturn-to-zero transmission setup. A scrambler that operates independent of its input polarization has also been realized. Both scramblers can be shared among a number of wavelength-division-multiplexed (WDM) channels for which PMD is to be detected. Furthermore, an inverse scattering technique has been implemented to determine differential group-delay profiles of an improved distributed PMD compensator in *X*-cut, *Y*-propagation LiNbO₃. In this context, the most common kind of higher order PMD is identified, which typically persists after compensation of first-order PMD. In a fiber link with polarization scrambling, it is shown to be measurable in a most efficient manner by comparing the rising and falling slopes of the detected signal using two oppositely poled one-way rectifiers placed at the output of a differentiator.

Index Terms—Optical fiber communication, optical fiber polarization, polarization-mode dispersion (PMD).

I. INTRODUCTION

POLARIZATION-MODE dispersion (PMD) continues to impair high-data-rate optical communication. Polarization scrambling facilitates first-order PMD detection [1]–[6] and has the potential of replacing spectral analysis of the detected base-band signal, in particular when it is combined with arrival time detection [1], [3], [6], which needs no extra optics in the receiver. Since the recovered clock phase automatically tracks the signal arrival time, it is sufficient to integrate the voltage-controlled oscillator input signal to obtain a measure of the arrival time variations and, hence, of PMD. Section II deals with the optimization of electrooptic polarization scramblers, including a version that operates independently of its input polarization and can most easily be shared among many wavelength channels.

The business case for 10-Gb/s PMD compensators (PMDCs) is relatively weak, because the substantial cost of one or more LiNbO₃ components must be justified in comparison with performance and cost of a regenerator. At 40 Gb/s, the situation is a lot more favorable: Regenerator cost is higher, more PMD needs to be compensated relative to the bit duration, and higher

order PMD compensation is, therefore, also much more important. However, first- and higher order PMD can be compensated in a single distributed PMDC in *X*-cut, *Y*-propagation LiNbO₃ [7], which we believe is the key to a cost-effective PMD compensation and merits further attention.

In Section III, the implementation of a proposed inverse scattering technique [8], [9] is being reported, and differential group-delay profiles are generated. In Section IV, that technique is applied to an improved version of the distributed PMDC [7] in order to investigate its compensation capabilities.

No compensation is possible without detection. Higher order PMD, which may persist after complete compensation of first-order PMD, is fairly difficult to detect, at least if low cost, high accuracy and short measurement intervals are desired. A solution is proposed in Section V. We describe how the most important kind or combination of higher order PMD can be measured in the electrical domain by slope difference detection, more sensitively than by simple spectral analysis or vertical eye-opening detection.

The subsequently described scramblers, distributed PMDC, and higher order PMD detection have not yet been combined into a 40-Gb/s PMD compensation system. We believe, however, that these progressive steps and arrival time detection of PMD will significantly increase performance and reduce the cost of a PMD compensation system when they are put together. The simple block diagram of Fig. 1 shows how the various enabling technologies could be combined for PMD compensation. The boldface boxes are dealt with in this paper. In a subsequent paper, we will describe how a larger number of voltages can be controlled efficiently in a distributed PMDC. A good starting point is certainly provided by the very sensitive arrival time detection of first-order PMD and the proposed slope difference detection.

II. OPTIMIZED POLARIZATION SCRAMBLERS

A. Single-Waveplate Scrambler for Circular Input Polarization

A variety of first-order PMD detection techniques [1]–[6] need polarization scramblers. Among these, we consider arrival time detection [1], [3], [6] to be most advantageous. In this section, we optimize such scramblers. It should be mentioned that scramblers must meet certain optical input power specifications if they are to scramble many wavelength channels simultaneously.

Now we shall derive the electrooptical requirements to be fulfilled by a polarization scrambler. Let the time-variable

Manuscript received September 19, 2002; revised November 18, 2002. This work was supported in part from Siemens ICN and from Deutsche Forschungsgemeinschaft. Part of this material has recently been presented at ECOC 2002 [10].

The authors are with the Optical Communication and High-Frequency Engineering University of Paderborn, 33098 Paderborn, Germany.

Digital Object Identifier 10.1109/JLT.2003.811563

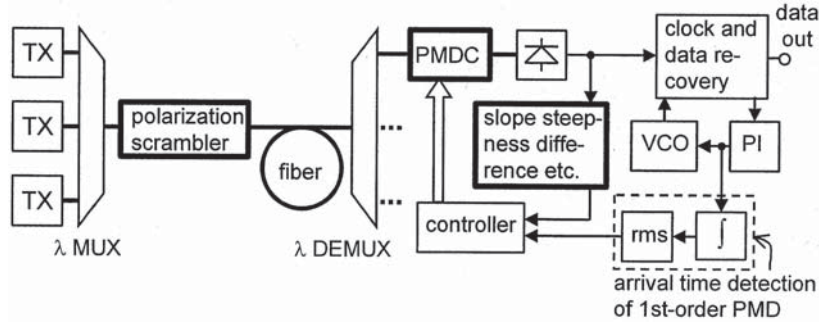


Fig. 1. Perspective showing how various enabling techniques should be combined for optical PMD compensation. TX = transmitters; λ MUX/DEMUX = wavelength-division (de)multiplexer; VCO = voltage-controlled oscillator; PI = proportional-integral controller of clock recovery PLL; and rms = root mean square.

scrambler output polarization and a principal state-of-polarization (PSP) of a subsequent fiber be denoted by the normalized Stokes' vectors $\mathbf{S}_{SC}(t)$ and \mathbf{S}_{PSP} , respectively. For a differential group delay (DGD) τ , the pulse arrival time is

$$\Delta\hat{t}(t) = \left(\frac{\tau}{2}\right) \mathbf{S}_{PSP}^T \mathbf{S}_{SC}(t) \quad (1)$$

where T denotes transposition. We drop the time (t) dependence and introduce the averaging operator $\langle \cdot \rangle$. The variance of $\Delta\hat{t}$

$$\sigma_{\Delta\hat{t}}^2 = \langle (\Delta\hat{t} - \langle \Delta\hat{t} \rangle)^2 \rangle = \left(\frac{\tau}{2}\right)^2 \mathbf{S}_{PSP}^T \cdot \mathbf{C} \cdot \mathbf{S}_{PSP} \quad (2)$$

depends on the covariance matrix

$$\mathbf{C} = \langle (\mathbf{S}_{SC} - \langle \mathbf{S}_{SC} \rangle) (\mathbf{S}_{SC} - \langle \mathbf{S}_{SC} \rangle)^T \rangle \quad (3)$$

of the scrambler output polarization. To maximize $\sigma_{\Delta\hat{t}}^2$ for all \mathbf{S}_{PSP} , the minimum eigenvalue of the positive semidefinite matrix \mathbf{C} must be maximized. In the optimum case, the average $\langle \mathbf{S}_{SC} \rangle$ vanishes, and \mathbf{C} becomes $\langle \mathbf{S}_{SC} \mathbf{S}_{SC}^T \rangle$ and equals $1/3$ times the identity matrix $\mathbf{1}$. Obviously, its three eigenvalues are all equal to $1/3$. One possible solution to achieve $\mathbf{C} = \mathbf{1}/3$ is an equidistribution of \mathbf{S}_{SC} on the Poincaré sphere. However, the corresponding scrambling period would be very long. In a receiver with arrival time detection, the arrival time fluctuations have to be measured over an integer number of scrambling periods or over a very long time. This guarantees a stable first-order PMD readout. A short measurement interval, equal to one scrambling period, is desirable in order to allow fast PMD detection. Harmonic signals are best suited to keep the scrambling period small, and they will result in \mathbf{S}_{SC} , describing a closed line on the Poincaré sphere.

We shall use only a single electrooptic waveplate in X-cut, Z-propagation LiNbO₃ [11] to implement such scramblers. These scramblers are particularly useful if all WDM channels

have equal polarizations, or if channels with like and orthogonal polarizations are interleaved in the frequency domain. Circular input polarization is required. A quarter-wave plate on the same chip can be used to convert horizontal/vertical linear polarizations into the right/left circular polarizations needed for scrambling.

In the scrambler, a TE-TM phase shift angle φ_{PS} and a TE-TM mode conversion angle φ_{MC} are applied together to produce a retardation $\varphi = \sqrt{\varphi_{PS}^2 + \varphi_{MC}^2}$ between linearly polarized eigenmodes having the normalized Stokes vectors $\pm[\varphi_{PS}/\varphi \ \varphi_{MC}/\varphi \ 0]^T = \pm[\cos\zeta \ \sin\zeta \ 0]^T$. Such a device is called a Soleil-Babinet compensator (SBC). The orientation angle ζ on the equator of the Poincaré sphere is twice the physical azimuth angle of an eigenmode. In the normalized Stokes space the output vector \mathbf{S}_{SC} is obtained by rotating the circular input polarization vector $\pm[0 \ 0 \ 1]^T$ by the retardation angle φ about the eigenmode axis. Mathematically, this is given by (4), shown at the bottom of the page, where the matrix describes the rotation. The rotation matrix is equal to what will subsequently be abbreviated as $\text{SBC}(\varphi, \zeta)$. More details regarding retarders can be found in [7]. One possible attempt to fulfill the condition $\mathbf{C} = \mathbf{1}/3$ is the following: The device is driven by voltages having as few harmonics as possible, in order to simplify driving. Two harmonics numerically optimized in phase (= cosine) and quadrature (= sine) amplitudes of both φ_{PS} and φ_{MC} are sufficient to very nearly fulfill the condition $\mathbf{C} = \mathbf{1}/3$. The ratio of the highest needed driving frequency divided by the fundamental scrambling frequency should be kept as low as possible to make scrambling fast, while keeping the harmonics content of the generated Stokes vector components low. This goal is reached by choosing the first and the second harmonic. The numerically optimized solution is

$$\begin{aligned} \varphi_{PS} &= (1.17 \pm 0.19) \sin \omega t + (1.17 \mp 0.19) \sin 2\omega t \\ \varphi_{MC} &= (1.17 \pm 0.19) \cos \omega t - (1.17 \mp 0.19) \cos 2\omega t \end{aligned} \quad (5)$$

$$\mathbf{S}_{SC} = \begin{bmatrix} \frac{\varphi_{PS}^2}{\varphi^2} + \frac{\varphi_{MC}^2}{\varphi^2} \cos \varphi & \frac{\varphi_{PS}\varphi_{MC}}{\varphi^2}(1 - \cos \varphi) & \frac{\varphi_{MC}}{\varphi} \sin \varphi \\ \frac{\varphi_{PS}\varphi_{MC}}{\varphi^2}(1 - \cos \varphi) & \frac{\varphi_{MC}^2}{\varphi^2} + \frac{\varphi_{PS}^2}{\varphi^2} \cos \varphi & -\frac{\varphi_{PS}}{\varphi} \sin \varphi \\ -\frac{\varphi_{MC}}{\varphi} \sin \varphi & \frac{\varphi_{PS}}{\varphi} \sin \varphi & \cos \varphi \end{bmatrix} \begin{bmatrix} 0 \\ 0 \\ \pm 1 \end{bmatrix} \quad (4)$$

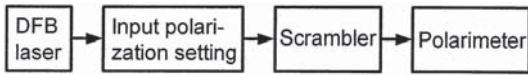


Fig. 2. Experimental setup for scrambler characterization.

where either the upper or the lower signs have to be chosen. Both generate S_{SC} patterns with a 120° rotation symmetry about the circular (S_3) axis of the Poincaré sphere [12].

A second, and better, attempt to achieve $C = 1/3$ consists in narrowing the spectral content of the Stokes parameters. A low harmonic number of the Stokes parameters is desirable, because it makes it easier for the receiver (RX) clock recovery to track the arrival time variations. This is important to avoid a scrambler-induced PMD penalty. It also enables the choice of a high ω , which means that the time interval necessary for PMD detection becomes short. A suitable output polarization trajectory is

$$\mathbf{S}_{SC} = \begin{bmatrix} S_{SC,1} \\ S_{SC,2} \\ S_{SC,3} \end{bmatrix} = \begin{bmatrix} \frac{(1 \pm \sqrt{\frac{1}{3}}) \cdot \cos \omega t - (1 \mp \sqrt{\frac{1}{3}}) \cdot \cos 3\omega t}{2} \\ \frac{(1 \pm \sqrt{\frac{1}{3}}) \cdot \sin \omega t + (1 \mp \sqrt{\frac{1}{3}}) \cdot \sin 3\omega t}{2} \\ \sqrt{\frac{2}{3}} \cdot \cos 2\omega t \end{bmatrix} \quad (6)$$

where, again, either all upper or all lower signs have to be chosen. The corresponding retardations can be obtained by inverting the three scalar equations contained in (4): Using the required overall retardation

$$\varphi = \arccos S_{SC,3} \quad (7)$$

of the waveplate for circular input polarization and the eigenmode orientation angle

$$\zeta = \arg(\varphi_{PS} + j\varphi_{MC}) = \arg(-S_{SC,2} + jS_{SC,1}) \quad (8)$$

we calculate the phase-shifting and mode conversion retardations

$$\varphi_{PS} = \varphi \cos \zeta = \frac{-S_{SC,2} \arccos S_{SC,3}}{\sqrt{S_{SC,1}^2 + S_{SC,2}^2}} \quad (9)$$

$$\varphi_{MC} = \varphi \sin \zeta = \frac{S_{SC,1} \arccos S_{SC,3}}{\sqrt{S_{SC,1}^2 + S_{SC,2}^2}}$$

From (6), we insert the Stokes parameters using the upper signs to implement what may be called a “tennis ball” scrambler. It has been implemented and characterized more closely in the setup of Fig. 2. An extra waveplate was used to generate circular input polarization for the scrambler waveplate. Both electrooptic waveplates were part of a commercially available integrated polarization transformer. A polarimeter was connected to the device output. The resulting Poincaré sphere trace was recorded with a scrambling period of ~ 1 s for demonstration purposes (Fig. 3). It looks like the vulcanization line between the two halves of a tennis ball. In Fig. 3, the Stokes parameter axes are oriented as expected from theory, but in reality, there was an unspecified polarization transformation between scrambler and polarimeter. The eigenvalues of C turned out to be very close to the ideal values of $1/3$, with relative deviations from their mean of only $\pm 1.7\%$. At the same time, this is the ultimately achievable relative PMD detection accuracy. The residual degree of

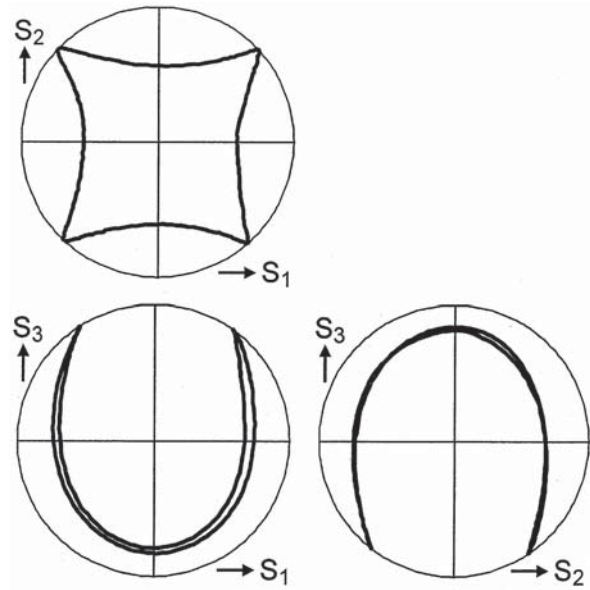


Fig. 3. Projections of the measured output polarization trace of a single-waveplate polarization scrambler.

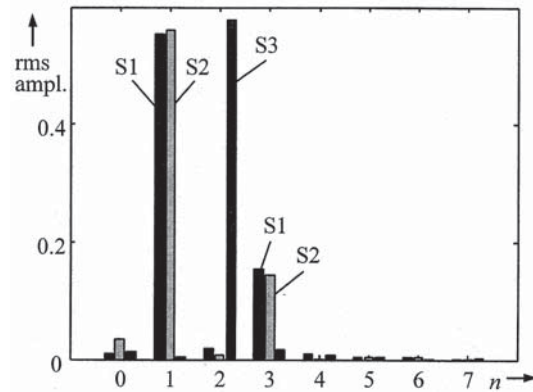


Fig. 4. Experimental harmonics amplitude spectra of the three normalized Stokes' parameters. They closely agree with theory ((6), using the upper signs).

polarization was almost zero, $\langle S_{SC} \rangle = 0.038$. The recorded Stokes parameter spectra are shown in Fig. 4. Depicted are the rms amplitudes of Stokes parameters measured at different multiples $n\omega$ of ω . As expected, the spectra are very clean. Almost all power is contained in the harmonics $n = 1, 3$ (both for S_1, S_2) and $n = 2$ (for S_3), respectively.

In the LiNbO_3 component differential time delays rather than constant retardations occur. This means that the retardations are proportional to the optical frequency. Therefore, optimum scrambler behavior can be expected only at one wavelength. The experimental driving voltage parameters were chosen for optimized performance at 1550 nm.

Next, the optical wavelength was varied. In Fig. 5, the three eigenvalues of C are displayed as a function of wavelength on either side of 1550 nm. Within a 4-THz optical bandwidth, the scrambling quality is sufficient.

The dynamic performance of the tennis ball scrambler has been assessed in a 40-Gb/s nonreturn-to-zero (NRZ) transmission setup (Fig. 6). The fundamental scrambling frequency

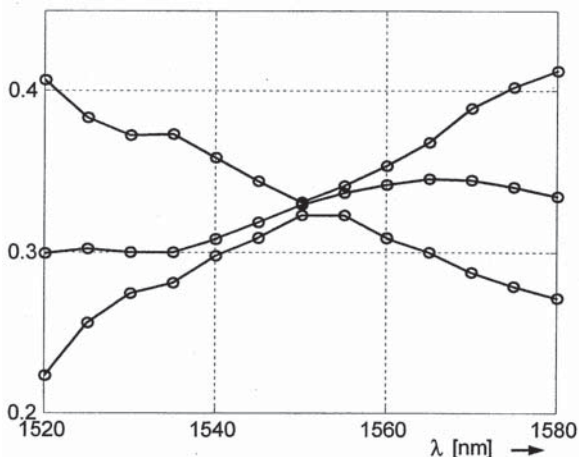


Fig. 5. Eigenvalues of covariance matrix C as a function of wavelength.

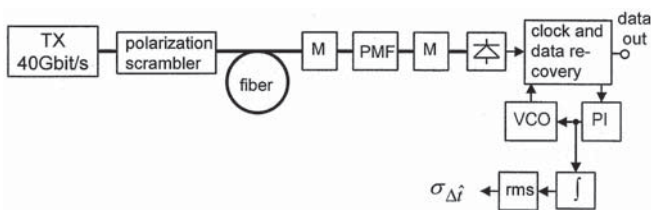


Fig. 6. First-order PMD detection using tennis ball scrambler and arrival-time detection. M = motorized endless fiber-optic polarization transformers.

was chosen to be 417 kHz. The measurement interval was one scrambling period, 2.4 μ s. Polarization-maintaining fiber (PMF) pieces were used as PMD devices under test. In order to include any uncontrollable polarization influence, including PDL, slow motorized polarization transformers (M) were inserted before and after the PMF.

The measured rms arrival-time variation $\sigma_{\Delta t}$ as a function of DGD is given in Fig. 7. The readouts for most favorable and unfavorable settings of the motorized polarization transformers are given, with added error bars of \pm one standard deviation. Above 1 ps, the measurement characteristics are very linear. If the highest readout without DGD is compared with the worst-case readout with DGD, the error intervals cease to overlap for 1.35 ps of DGD, which may be considered to be the detection sensitivity. However, one may as well argue that the polarization transformation between the scrambler and the input of a PMD compensator stay the same while first-order PMD is being minimized by this PMD compensator. If this is true, one must compare the readouts for zero and nonzero DGDs of a particular case (the worst). That sensitivity definition showed nonoverlapping error intervals for a DGD of 880 fs. The achieved sensitivity, near 1 ps, depending on definition, and the short measurement interval are believed to be a key for fast and accurate PMD compensation. Given the fact that the initially used polarimeter was a low-speed instrument, one may even hope to narrow the gap between highest and lowest PMD readouts if a high-speed polarimeter is used to set up the scrambler.

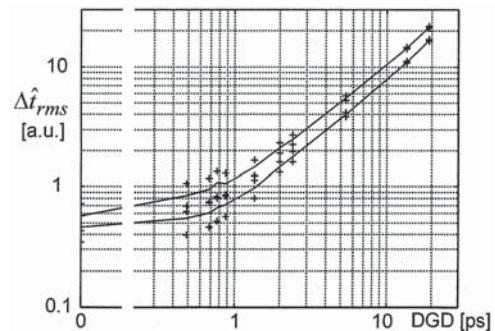


Fig. 7. PMD detection readout for tennis ball scrambler. Solid curves correspond to lowest and highest readouts caused by motorized polarization transformers. Associated \pm one-standard-deviation intervals are indicated by “+”.

B. Dual-Waveplate Polarization-Independent Scrambler

System design would be eased if the scrambler operated completely independent of its input polarization. Therefore, we now seek that C be equal to $1/3$ times the identity matrix not just for one, but for all scrambler input polarizations. A particular solution to this problem is a retarder with a retardation of $\epsilon = \pi - \arccos(7/8)$ and eigenmodes that are equidistributed on the Poincaré sphere. This can easily be verified. As an example, one could use two electrooptic waveplates as SBCs in the following way. The waveplates are operated with equal retardations φ having a sinelike probability density function in the interval $[0; \pi]$. Both waveplates are rotated in the same direction at the same speed, but their eigenmode orientation angles ($=$ twice the azimuth angle) $\zeta, \zeta + \pi$ differ by π on the Poincaré sphere equator. Each of these waveplates would transform circular polarization into a polarization equidistributed on the Poincaré sphere. Between the waveplates, there must be a circular retarder with a retardation of ϵ . This can be an $\epsilon/2$ physical rotation. The two electrooptic waveplates operate inversely to each other due to the orientation angle difference and, therefore, transform the circular ϵ retardation into an ϵ retardation with eigenmodes equidistributed on the Poincaré sphere, as required. We illustrate this configuration at the top of Fig. 8. The first and second argument of the “SBC” denotes retardation and orientation angle, respectively. The circular retarder is denoted by “C” and its retardation as argument.

If arbitrary constant retarders are added before and/or behind this particular retarder, the scrambling action will not be compromised. With such constant retarders added, the general solution to the polarization-independent scrambler problem is indeed obtained. Here is a possible implementation: In the previous example, we add another circular retarder with a retardation of $-\epsilon$ after the second electrooptic waveplate at the scrambler output, as shown in the middle of Fig. 8. The two circular retarders and the second electrooptic waveplate between them can be replaced by an electrooptic waveplate with the same retardation as before but with an orientation angle that differs by $-\epsilon$ on the Poincaré sphere equator from its original value (see Fig. 8, bottom). Therefore, it differs only by $\pi - \epsilon$ from the orientation angle of the first electrooptic waveplate. We summarize the end product of this metamorphosis:

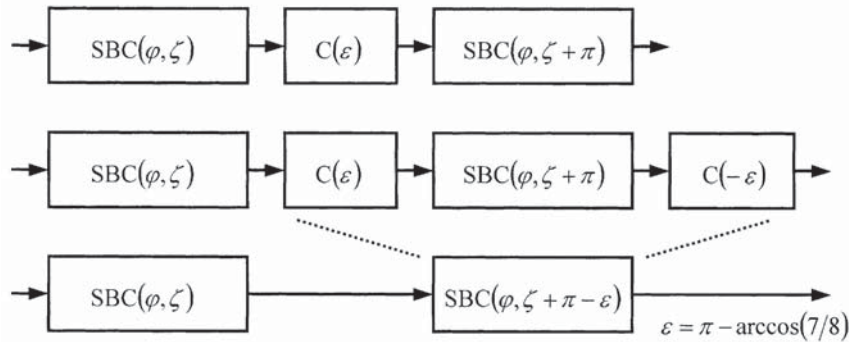


Fig. 8. Implementation of scramblers that operate independently of input polarization (see text).

Two concatenated waveplates are operated with equal retardations having a sinelike probability distribution in the interval $[0; \pi]$. Both waveplates are rotated in the same direction at the same speed, but their orientation angles differ by $\pi - \epsilon \approx 0.5$ rad on the Poincaré sphere equator. Retardation(s) and orientation angle(s) have to be chosen statistically independent.

If implemented as described, the scrambler requires an infinite scrambling period, which is unrealistic. In order to obtain a finite scrambling period, we use the approximation

$$\begin{aligned} \varphi_{PS1} &= A - B, & \varphi_{PS2} &= A + B \\ A &= 0.28 \cdot \sin \omega t - 1.15 \cdot \sin 3\omega t + 0.82 \cdot \sin 4\omega t \\ B &= 0.26 \cdot \cos \omega t + 0.37 \cdot \cos 3\omega t + 0.14 \cdot \cos 4\omega t \\ \varphi_{MC1} &= C - D, & \varphi_{MC2} &= C + D \\ C &= -0.99 \cdot \cos \omega t - 1.40 \cdot \cos 3\omega t - 0.52 \cdot \cos 4\omega t \\ D &= 0.07 \cdot \sin \omega t - 0.31 \cdot \sin 3\omega t + 0.22 \cdot \sin 4\omega t \quad (10) \end{aligned}$$

where the indexes 1, 2 denote the two waveplates. It was found by a numerical optimization scheme. The eigenvalues of \mathbf{C} were determined for all possible scrambler input polarizations, and the parameters, whose final values show up in (10), were varied to maximize the minimum eigenvalue found among all input polarizations.

Experimentally, two adjacent waveplates on the same chip were used for scrambling. Another waveplate with circular input polarization generated a grid of 51 scrambler input polarizations, fairly equidistributed on the whole Poincaré sphere. The covariance matrix \mathbf{C} was measured, and its eigenvalues were determined, separately for each input polarization. A histogram of the eigenvalues is shown in Fig. 9. The minimum of the smallest eigenvalue was > 0.26 . The maximum of the largest eigenvalue was < 0.35 . Therefore, the achievable relative accuracy of an arrival time-based PMD detector will ideally vary by just $\pm 15\%$, depending on scrambler input polarization and principal states-of-polarization of the fiber. If a PMD compensator is used, it can be expected to exhibit the same amount of variation in its convergence speed. As long as the minimum convergence speed is high enough, the variations should not matter too much.

The scrambled Stokes parameter spectra depend on the scrambler input polarization. The spectra of the three normal-

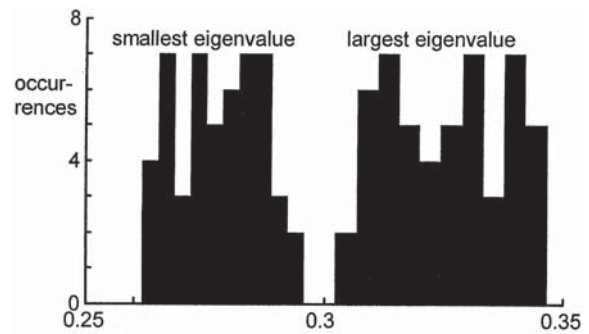


Fig. 9. Histograms of largest and smallest eigenvalue of 51 covariance matrices.

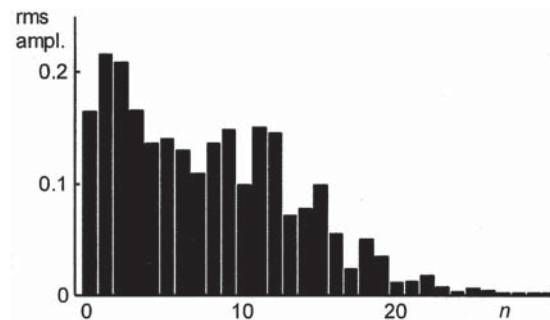


Fig. 10. Harmonics amplitudes at output, averaged over all Stokes' parameters and input polarizations.

ized output Stokes parameters were first determined for each input polarization. Then, their squared magnitudes, i.e., the corresponding power spectra, were averaged over all input polarizations and all three Stokes' parameters, in order to reduce the enormous amount of data. In Fig. 10, the amplitudes of the resulting spectrum are plotted. Although there is no direct physical significance of this plot, it is clear that there are more harmonics as a price to pay for the advantage of being (fairly) polarization-insensitive. A large clock recovery PLL bandwidth must be recommended for arrival time detection of PMD.

The wavelength dependence of the smallest and largest eigenvalue of \mathbf{C} was also assessed (Fig. 11). The scrambling quality can be considered to be sufficient in a 4-THz bandwidth.

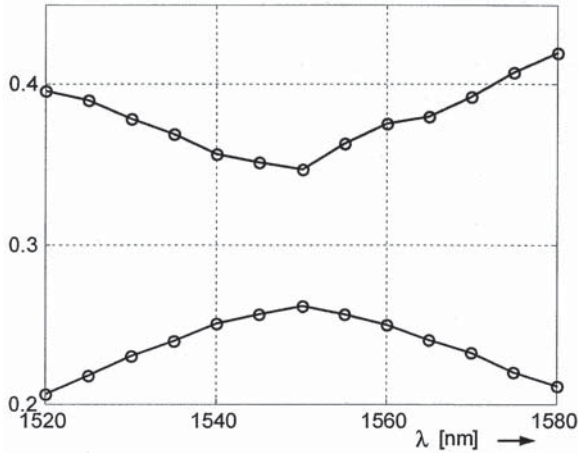


Fig. 11. Smallest and largest eigenvalue of covariance matrix at all input polarizations, as a function of wavelength.

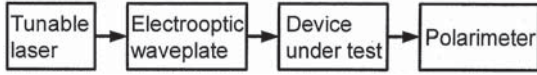


Fig. 12. Experimental setup for DGD profile measurement.

III. DGD PROFILE MEASUREMENT

A. Jones Matrix Measurement

PMD in fibers is conveniently modeled by a concatenation of DGD sections connected by variable mode converters. Jones or Müller matrix measurement over optical frequency has enabled the verification of the structure of a medium with three DGD sections [13] and of the PMD vector and its derivative with respect to optical frequency [14]. An inverse scattering algorithm was detailed by Möller [8], generalizing early work by Harris *et al.* [9]. Experimental validation seems not to have been reported so far, nor does a PMD medium with complicated structure seem to have been analyzed. The method would be of particular help for nondestructive characterization of distributed PMDCs.

A pigtailed electrooptic waveplate [11] was fabricated in X-cut, Z-propagation LiNbO₃. It was connected to a tunable laser (Fig. 12) and driven to periodically generate eight polarization states dispersed on the whole Poincaré sphere. These were launched into a device under test (DUT). A polarimeter was connected to the DUT output. The laser was swept in 10-GHz steps between 1525 nm and 1545 nm, and within this range, it had no mode hops. The frequency-dependent 3×3 rotation matrix \mathbf{R} of the device, i.e., the lines and columns 2 to 4 of its Müller matrix, were thereby determined. Each of the n ($= 8$ in our case) normalized input (in) Stokes vectors corresponds to a certain output (out) Stokes vector, thereby forming a $3 \times n$ matrix. Both vector groups are arranged in form of a matrix equation

$$\mathbf{S}_{\text{out}} = \mathbf{R} \mathbf{S}_{\text{in}}. \quad (11)$$

The rotation matrix \mathbf{R} is then obtained by

$$\mathbf{R} = \mathbf{S}_{\text{out}} \mathbf{S}_{\text{in}}^T (\mathbf{S}_{\text{in}} \mathbf{S}_{\text{in}}^T)^{-1}. \quad (12)$$

Our choice of \mathbf{R} minimizes the errors introduced during polarization measurement in a least-square sense. Compared with the compact method [14], with only two launched polarizations, the multiple polarizations yield a better immunity against measurement errors. Any residual nonorthogonality of \mathbf{R} is removed by a singular value decomposition of \mathbf{R} according to

$$\mathbf{R} = \mathbf{u} \mathbf{s} \mathbf{v}^+ \quad (13)$$

where \mathbf{u} , \mathbf{v} are orthogonal (or, more generally, unitary) matrices, and \mathbf{s} is a diagonal matrix containing the singular values. \mathbf{R} is then redefined as an orthogonal matrix

$$\mathbf{R} := \mathbf{u} \mathbf{v}^+. \quad (14)$$

From this new \mathbf{R} , the frequency-dependent Jones matrix was obtained in the form $\mathbf{J} = \begin{bmatrix} A & B \\ -B^* & A^* \end{bmatrix}$, $|A|^2 + |B|^2 = 1$, using the equations

$$\begin{aligned} K_{11} &= \sqrt{\left(\frac{1}{2}\right) (1 + R_{11})} \\ K_{22} &= \left(\frac{1}{2}\right) \frac{((R_{22} + R_{33}) - j(R_{32} - R_{23}))}{K_{11}} \\ K_{12} &= \left(\frac{1}{2}\right) \frac{(R_{12} + jR_{13})}{K_{11}} \\ K_{21} &= \left(\frac{1}{2}\right) \frac{(R_{21} - jR_{31})}{K_{11}} \\ \mathbf{J} &= \begin{bmatrix} K_{11} & K_{12} \\ K_{21} & K_{22} \end{bmatrix} \cdot e^{-(j/2) \cdot \arg(K_{22})}. \end{aligned} \quad (15)$$

There are always two valid solutions at a specific frequency, \mathbf{J} and $-\mathbf{J}$. It is necessary to select the correct one. If the sign changes between adjacent frequency points, the impulse response will be distorted due to an introduced severe chromatic dispersion. The correct sign is found if \mathbf{J} is as smooth as possible in the frequency domain. In a specific frequency region, \mathbf{J} may be diagonally dominated ($|A| > |B|$) or not ($|A| \leq |B|$). When moving in the frequency domain from one sample $\mathbf{J}(\omega_k)$ to the next sample $\mathbf{J}(\omega_{k+1})$, the sign of $\mathbf{J}(\omega_{k+1})$ must be chosen so that the dominating one of the elements A_{k+1} , B_{k+1} has the lowest possible phase difference to its neighbor A_k , B_k , respectively. This means that if $|A_{k+1}| > |B_{k+1}|$ and $\arg(A_{k+1}A_k^*) > \pi/2$ hold, the sign of $\mathbf{J}(\omega_{k+1})$ must be inverted. It must also be inverted if $|A_{k+1}| \leq |B_{k+1}|$ and $\arg(B_{k+1}B_k^*) > \pi/2$ hold.

The frequency-domain results were multiplied by a \cos^2 window centered at 1535 nm to suppress errors introduced by discontinuous borders. The window had its zeros at the borders 1525 and 1545 nm. The inverse of the free spectral range equaled 392 fs. Inverse Fourier transform resulted in a time-dependent Jones matrix with impulse responses as elements. Its first column is the finite-impulse response to a horizontally polarized input pulse.

Windowing in the frequency domain introduces correlations between neighbor samples in the time domain. The impulse response was therefore resampled with a doubled $\tau = 785$ -fs period.

B. Inverse Scattering Algorithm

After these preparatory steps, the structure is analyzed on the basis of sections having DGDs τ equal to this value of 785 fs. For a complete derivation of this layer-peeling algorithm, with a nomenclature slightly different from ours, the reader is referred to [8]. Here, we concentrate on implementation of the algorithm. The complete impulse response can be written as (16), shown at the bottom of the page.

From left to right, the product is executed with descending index i . The second expression serves to define the sequence of impulse weight vectors $\begin{bmatrix} h_{1,i} \\ h_{2,i} \end{bmatrix}$, which are needed in the following. Just prior to the multiplication from right onto the m th mode converter matrix, the x and y fields undergo a DGD τ in the $(m-1)$ th section. Therefore, the field components of the first sample and/or the last sample enable the determination of the retardation φ_m and the orientation angle ψ_m of the mode converter that is present at the DUT output. However, depending on the structure to be analyzed, one or the other of these samples may vanish. This problem is solved, and measurement errors occurring at both sides of the impulse response are best averaged out, if we take a weighted average of the information available at both ends of the impulse response. Suitable expressions are

$$\begin{aligned} \varphi_m &= 2 \arctan \frac{|h_{2,m-1}| + |h_{1,0}|}{|h_{1,m-1}| + |h_{2,0}|} \\ \psi_m &= \arg(jh_{1,m-1}h_{2,m-1}^* - jh_{1,0}h_{2,0}^*). \end{aligned} \quad (17)$$

Once this is known, the mode conversion effect can be removed from the overall impulse response via multiplication by a Jones matrix $\begin{bmatrix} \cos(-\varphi_m/2) & je^{j\psi_m} \sin(-\varphi_m/2) \\ je^{-j\psi_m} \sin(-\varphi_m/2) & \cos(-\varphi_m/2) \end{bmatrix}$ which is inverse to the m th-mode converter matrix. By this multiplication, the first sample of the impulse response is confined to field component 2 ($= y$), and the last sample is confined to the orthogonal field component 1 ($= x$). Now, a time backshift of the samples in one field component is possible. It neutralizes a DGD section with principal states-of-polarization (PSPs) equal to these field components, which precedes the already-known

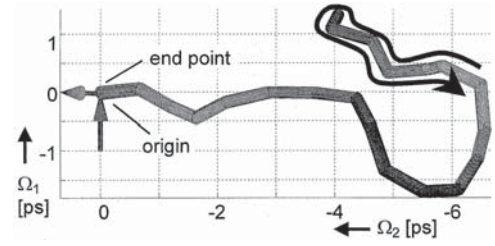


Fig. 13. DGD profile back-to-back. DGD sections run forward and backward along the same path, ending at origin. The turning point is where the curved arrow changes direction by 180° .

mode conversion. The pure time shift (without differential phase shift) means that the DGD section exhibits a retardation between the PSPs, which is an integer multiple of 2π at the center frequency of the optical scanning range. It has been shown in [19] that this is not a restriction. The impulse response is convolved from left by $\begin{bmatrix} \delta(t+\tau) & 0 \\ 0 & \delta(t) \end{bmatrix}$. The time backshift results in a new impulse response that is shorter by one sample. The process is repeated until a single impulse $\begin{bmatrix} \cos(\varphi_1/2) \\ je^{-j\psi_1} \sin(\varphi_1/2) \end{bmatrix} \delta(t)$ remains. It enables the determination of the initial mode conversion specified by φ_1, ψ_1 , which precedes the first DGD section. The impulse that generates the response, and all local slow PSPs, are assumed to be the horizontal (Ω_1 direction, marked by an input arrow in Figs. 13–18), because we have started from a Jones matrix in horizontal/vertical coordinates. Experimentally, the inverse scattering range was chosen as 31.4 ps (40 sections).

The k th-mode converter is specified by a rotation matrix in the cartesian Stokes space [see (18), shown at the bottom of the page]. SBA stands for Soleil–Babinet analog [19]. The rotation matrix of a DGD section with horizontal polarization as the slow PSP is

$$\mathbf{PS} = \begin{bmatrix} 1 & 0 & 0 \\ 0 & \cos \omega\tau & \sin \omega\tau \\ 0 & -\sin \omega\tau & \cos \omega\tau \end{bmatrix} \quad (19)$$

where \mathbf{PS} stands for phase shifter. The DGD or PMD profile of concatenated retarders is a concatenated sequence of input-

$$\begin{aligned} \mathbf{h}(t) &= \begin{bmatrix} \cos(\frac{\varphi_m}{2}) & je^{j\psi_m} \sin(\frac{\varphi_m}{2}) \\ je^{-j\psi_m} \sin(\frac{\varphi_m}{2}) & \cos(\frac{\varphi_m}{2}) \end{bmatrix} \\ &\cdot \prod_{i=m-1}^1 \left(\begin{bmatrix} \delta(t-\tau) & 0 \\ 0 & \delta(t) \end{bmatrix} * \begin{bmatrix} \cos(\frac{\varphi_i}{2}) & je^{j\psi_i} \sin(\frac{\varphi_i}{2}) \\ je^{-j\psi_i} \sin(\frac{\varphi_i}{2}) & \cos(\frac{\varphi_i}{2}) \end{bmatrix} \right) \begin{bmatrix} \delta(t) \\ 0 \end{bmatrix} \\ &= \sum_{i=0}^{m-1} \begin{bmatrix} h_{1,i} \\ h_{2,i} \end{bmatrix} \cdot \delta(t - i \cdot \tau). \end{aligned} \quad (16)$$

$$\mathbf{SBA}_k = \begin{bmatrix} \cos \varphi_k & -\sin \psi_k \sin \varphi_k & \cos \psi_k \sin \varphi_k \\ \sin \psi_k \sin \varphi_k & \cos^2 \psi_k + \sin^2 \psi_k \cos \varphi_k & \sin \psi_k \cos \psi_k (1 - \cos \varphi_k) \\ -\cos \psi_k \sin \varphi_k & \sin \psi_k \cos \psi_k (1 - \cos \varphi_k) & \sin^2 \psi_k + \cos^2 \psi_k \cos \varphi_k \end{bmatrix}. \quad (18)$$

referred PMD vectors $\tilde{\Omega}_i$ with $\tilde{\Omega}_i = \mathbf{R}_{<i}^T \Omega_i$. The transpose (T) of a rotation matrix is its inverse. The rotation matrix

$$\mathbf{R}_{<i} = \mathbf{SBA}_i \cdot \prod_{k=i-1}^1 (\mathbf{PS} \cdot \mathbf{SBA}_k) \quad (20)$$

represents all concatenated retarders preceding the retarder with local PMD vector Ω_i . For calculation of $\mathbf{R}_{<i}$ at arbitrary frequencies, not only the mode converters separating the DGD sections, but also the DGD sections themselves, having highly frequency-dependent retardations $\omega\tau$ between the PSPs, are taken into account.

Ω_i is the normalized Stokes vector of a PSP, multiplied by the DGD. This statement holds also for the total PMD vector $\tilde{\Omega}_{\text{total}} = \sum \tilde{\Omega}_i$, $\text{DGD}_{\text{total}} = |\tilde{\Omega}_{\text{total}}|$. In order to allow for a zero length of the last, say the m th, DGD section, we mark its direction by an output arrow. Its direction is $\mathbf{R}_{<m}^T [1 \ 0 \ 0]^T$. If it is multiplied onto the total rotation matrix $\mathbf{R}_{<m}$, the result is obviously $[1 \ 0 \ 0]^T$, and this is the local slow PSP of the last section. Therefore, the output arrow indicates that continuous-wave (CW) input polarization, which would be necessary to excite the local slow PSP of the last section.

The inverse scattering algorithm will always succeed and will always display a full-length DGD profile (40 sections). At first, a back-to-back measurement without DUT was performed (Fig. 13). The measured output polarization state was almost constant over the wavelength range. The corresponding impulse response is essentially a Dirac impulse in the center of a 41-sample-long impulse response. Initially, measurement noise will introduce random errors. After 20 sections, the (meanwhile mode-converted and dispersed) Dirac impulse components start to be used when (17) is executed. Note that (17) deals no longer with the original impulse response at that moment, and instead of $m = 41$, we have to take the index $m = 21$. When this happens, a full mode conversion is sensed, and subsequently, in the second half of the derived structure, all previously accumulated errors are canceled. Indeed, all PMD vectors (= rods) in Fig. 13 are canceled by oppositely directed adjacent ones. The DGD profile travels 20 sections forth and then another 20 sections back on the same path, as if returning from a dead end (see inserted curved arrow). As a consequence, one has the impression of seeing only 20 sections, which, in reality, hide the other 20 sections. The input arrow tip and output arrow tail coincide within < 100 fs, which is a measurement error, since the true DGD was $\ll 100$ fs. Therefore, the simplified back-to-back DGD profile reduces to a frequency-independent polarization transformation specified by the rotation between the two arrows.

Next, the DUT (Fig. 14) was an ~ 25 -ps piece of PMF. It yielded a straight 25.12-ps-long line (32 sections) followed by a short dead end (2×4 sections). Concatenation of two PMF pieces with ~ 22 and ~ 6 ps of DGD, respectively, and a 50% mode conversion (45° rotation) in between them resulted in the profile of Fig. 15. The long section and the short section, which also contains a short dead end (2×1 section), are clearly seen. The angle between the sections, which equals the SBA retardation, was $\sim 90^\circ$ as expected. Verified results from other fiber

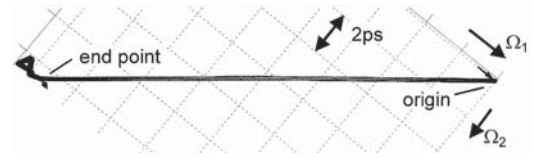


Fig. 14. DGD profile of one 25-ps DGD section. The Ω_3 component is not seen in this projection.

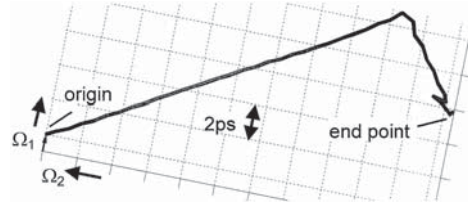


Fig. 15. DGD profile of two DGD sections (22 ps + 6 ps). The Ω_3 component is not seen in this projection.

DUTs are not available as of now. However, the next section of the paper shows the characterization of an integrated optic DUT.

IV. DISTRIBUTED PMD COMPENSATOR IN X-CUT, Y-PROPAGATION LiNbO₃

A distributed X -cut, Y -propagation LiNbO₃ PMD compensator can substitute a number of DGD sections and a number of concentrated polarization transformers at 40 Gb/s. A pigtailed, distributed PMD compensator was fabricated, similar to those in [7]. Seventy in-phase and quadrature TE-TM mode converters were distributed along a 94-mm-long waveguide. Control voltages $V_{1,k} \propto \varphi_k \cos \psi_k$ and $V_{2,k} \propto \varphi_k \sin \psi_k$ mediate quadrature and in-phase mode conversion in the k th SBA, respectively, and can bend the DGD profile independently in two orthogonal directions, perpendicular to the local DGD profile direction. The SBA must be defined to contain a waveguide section with an integer number of beat lengths. The retardation components $\varphi_k \cos \psi_k \propto V_{1,k}$ and $\varphi_k \sin \psi_k \propto V_{2,k}$ may be called quadrature and in-phase mode conversion retardations, respectively, because the mode-converted wave is either in quadrature or in phase with the original wave. The total retardation and orientation angles of the SBA are $\varphi_k \propto \sqrt{V_{1,k}^2 + V_{2,k}^2}$ and $\psi_k = \arg(V_{1,k} + jV_{2,k})$, respectively.

The device loss was 4 dB, and the PDL was 1.1 dB. The mode conversion efficiency is conveniently defined for the case where either $V_{1,k}$ or $V_{2,k}$ is applied, i.e., mode conversion in a single quadrature. The required voltage times length product for full mode conversion, with half of the length that belonged to the other quadrature being unused, was 375 V·mm. This improvement over the previously reported figure of 250 V·mm (assuming that only one type of mode converter electrode is there) or 500 V·mm (when using the previously given efficiency definition) [7] was due to a thinner buffer layer. The total DGD was about 25 ps. Without any voltages applied, the DGD profile was similar to that of Fig. 13. With the exception of the folded dead end, a straight line would be expected as the DGD profile, but in reality, a gentle bend was observed. The center of the DGD profile bend deviated by ~ 1 ps from a straight line connecting start and endpoint of the bend. Therefore, the bend was very gentle.

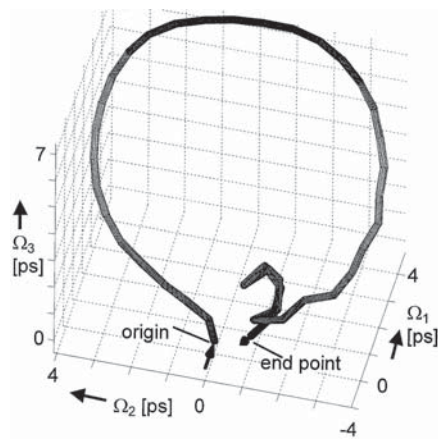


Fig. 16. DGD profile of LiNbO₃ PMDC with two full mode conversions distributed over the whole length.

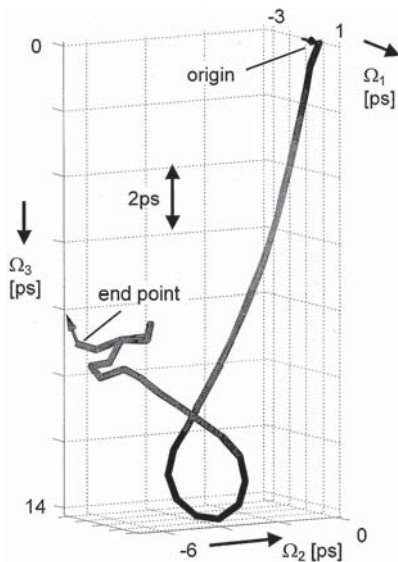


Fig. 17. DGD profile of LiNbO₃ PMDC with 1.5 full mode conversions after about 17 ps of DGD.

For another case, Fig. 16 shows the DGD profile bent to form a full circle. This means that all SBAs have the same orientation angles $\psi_1 = \psi_2 = \dots$. The mode conversions occur between locally x - and y -polarized waves in the chip. Therefore, Fig. 16 shows two full mode conversions (two bends by 180° each) in one quadrature (i.e., all portions of the bends lie in the same plane), and these are distributed along the whole chip. Due to an additional polarization transformation in the input fiber of the chip, there is a direction change between the input arrow and the first DGD sections. A dead end with approximately 2×4 sections is also seen, because the total DGD value of the chip was less than the inverse scattering range. In yet another example with differently chosen voltages, the pigtail-shaped profile of Fig. 17 was obtained. It displays 1.5 full mode conversions, but they are concentrated at about $3/4$ of the total DGD. This demonstrates the versatility of the distributed PMD compensator.

The inverse scattering technique can be employed online (with live data traffic) only in polarization diversity coherent optical receivers, which enable the measurement of the impulse

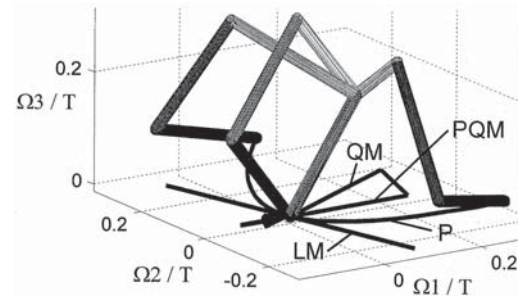


Fig. 18. PMD profile for vanishing first-order PMD. Output arrows are not shown for easier visibility.

response by correlation techniques. Here, it serves only to characterize a PMD compensator offline.

V. SLOPE STEEPNESS DETECTION

Any highly sensitive first-order PMD detection scheme, such as arrival-time detection, needs polarization scrambling. We now consider this scenario, assuming that first-order PMD is completely eliminated by a PMD compensator. This means that the origin and endpoint of the resulting DGD profile coincide at the carrier frequency. The DGD profile will therefore most likely consist of a loop or a similar closed trajectory.

Fig. 18 shows such a profile, composed here of four DGD sections with lengths of $0.25T$ each ($T =$ bit duration). Its three different instantiations are taken below the carrier frequency ($=$ one of the open loops), at the carrier frequency ($=$ the closed loop), and above the carrier frequency ($=$ the other open loop). The differences between the off-carrier frequencies and the carrier are $\pm 1/(2T)$. For a constant DGD of a section, the retardation between the PSPs is proportional to the optical frequency. Each DGD section therefore twists about its axis as a function of optical frequency, and the following remainder of the DGD profile is rotated about that axis. The first DGD section stays at the same place for all frequencies, because it is preceded only by a frequency-independent polarization transformation. The calculated profile endpoint describes roughly a parabola (P) as a function of optical frequency. The overall PMD vector itself starts from the coordinate origin and ends on a point of the parabola. In this example, the overall PMD vectors, i.e., the DGD profile endpoints, at the three frequencies having offsets of $-1/(2T)$, $0/T$ and $1/(2T)$ with respect to the carrier, are $T \cdot [0.33 \ -0.16 \ 0.02]^T$, $T \cdot [0 \ 0 \ 0]^T$, and $T \cdot [0.15 \ 0.33 \ 0.04]^T$, respectively. The parabola is composed of a linear motion along an abscissa (LM), which distorts the signal like chromatic dispersion, and a quadratic motion along an ordinate (QM) perpendicular to LM. Fig. 19 shows simulated eye diagrams back to back (top left) and three more for various polarization transformations added at the input of the medium, which is otherwise described by Fig. 18. In these three, QM is perpendicular (top right), equal (bottom left), or opposed (right) to the input polarization direction.

The closed-loop case is less special than it might seem: If the DGD profile loop occupies one plane but is not closed, or if there are only two DGD sections, such as in Fig. 15, the situation will, in principle, be very similar to the closed-loop case. However, first-order PMD can mask most effects unless the input

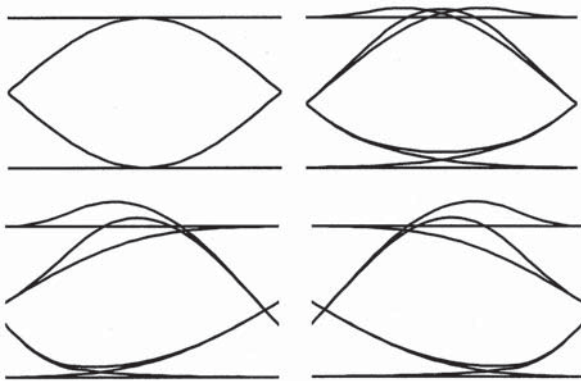


Fig. 19. Simulated eye diagrams back to back (top left), with unequal slopes (bottom) and with unequal curvatures (all except back to back).

polarization coincides with the PSP of the overall DGD profile. In the two-section case, the profile endpoint will rotate on a circle, which can be approximated near the carrier frequency by a parabola.

Next we discuss the effects of a DGD profile loop on the eye diagram. These, as well as subsequent findings, were verified based on additional simulations and calculations.

We start with the linear motion LM of the DGD profile endpoint as a function of optical frequency. The projection of LM along the input polarization (arrow into origin) direction indicates a quadratic dependence of the phase or a linear dependence of the group delay on the optical frequency, i.e., a *polarization-dependent* chromatic dispersion [15], [16]. In reality, both polarizations are subject to it independently but with different signs. Therefore, the magnitude of the derivative of LM (= the speed at which the DGD profile endpoint moves) matters, but its direction does not matter, as long as first-order PMD is small enough and as fiber chromatic dispersion does not introduce a further, *polarization-independent* quadratic-phase dependence as an offset.

In general, the combination of fiber and PMD-induced chromatic dispersion is most easily measured by comparing positive and negative curvatures of the detected signal. This is possible if the received electrical signal is differentiated twice (Fig. 20, top). Two attached one-way rectifiers yield mean 1 and 0 symbol curvatures, with different signs. Their sum, i.e., the curvature difference, depends linearly on the speed of LM. We have modeled the rectifiers to yield the mean square of either the positive or the negative portions of the signal. This means that they may be considered to be ideal rectifiers followed by squarers and low-pass filters.

But what about QM? QM indicates a cubic dependence of the phase or a quadratic dependence of the group delay on the optical frequency, just like the so-called third-order chromatic dispersion. Depending on the sign of that dependence, there is an eye diagram shear where rising signal slopes are steeper than falling signal slopes, or vice versa (see also [17] for an illuminating discussion on the related issue of chromatic dispersion). Her, this sign depends on the input polarization (or the DGD profile loop orientation). The same kind of eye-diagram shear was found for another DGD profile which, at the carrier frequency, is shaped like a written “figure eight” (two loops with opposite curvature) and starts at the center of the eight. As a

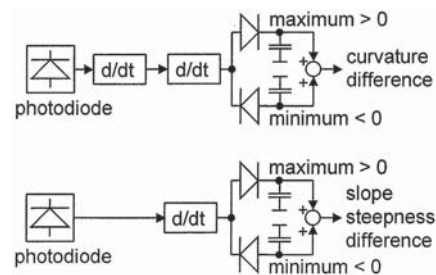


Fig. 20. Curvature difference (top) and slope steepness difference (bottom) estimation of detected signal.

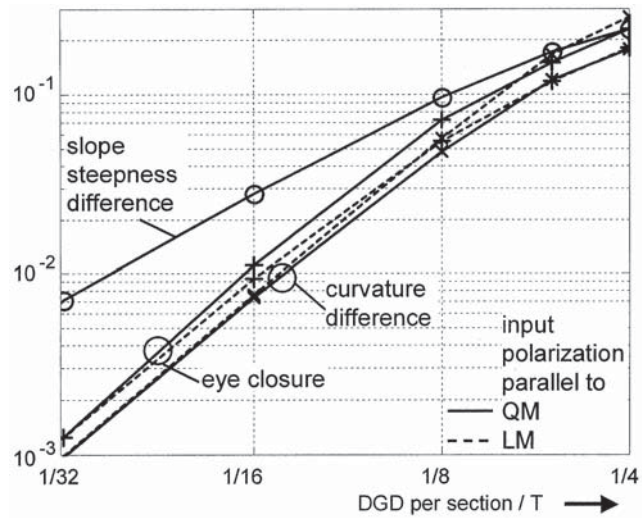


Fig. 21. Simulated readouts provided by eye closure (+), slope steepness difference (o), and curvature difference (x) measurement as a function of section length in a square-shaped DGD profile. All quantities are normalized.

function of optical frequency, that profile generates approximately no LM but only QM. In all these and in a number of other investigated examples, it was found that *it is the projection (PQM) of QM along the input polarization that determines magnitude and sign of the slope steepness difference*. In particular, if the DGD profile loop of Fig. 18 is reoriented so that PQM vanishes, the slope difference disappears, and only the curvature difference persists. For slope difference measurement, one of the two differentiators simply has to be left out (Fig. 20, bottom). The one-way rectifiers yield mean 01 and 10 symbol transition slope steepnesses, with different signs. According to all our simulations, their sum depends roughly linearly on PQM, including sign.

Polarization scrambling rotates the profile and lets PQM oscillate because the direction of QM is modulated in the PMD vector space. The PMD compensation algorithm, together with the PMDC, must try to make these oscillations vanish. If the dynamic part of the eye shear vanishes at all times, QM is zero, there is no DGD profile loop, and the associated higher order PMD is compensated.

In terms of traditionally defined [18] PMD orders, the linear motion LM is a second-order effect, and it is proportional to the square of the DGD section length. The quadratic motion QM is a third-order effect, and is proportional to the cube of the DGD section length. Fig. 21 shows simulated slope difference and curvature difference readouts, in each case normalized to

TABLE I
PROPERTIES OF DIFFERENT METHODS FOR THE DETECTION OF AN ARBITRARILY ORIENTED DGD PROFILE LOOP

Measurement of	eye opening	highpass filter output power	curvature difference	slope steepness difference
Detects PMD of order	1, 2, 3	1, 2, and, with wrong sign, 3	2, 3	3
Readout is \propto DGD ⁿ , n =	3	ambiguous readout (see above)	3	2
Hardware effort	highest	low	higher	low
Speed	slow	fast	fast	fast
Patterning		strong		weak
Polarization scrambler needed?		no		yes
Influence of fiber chromatic dispersion (CD)	polarization-dependent addition of 2nd-order PMD and fiber CD			decreases readout

the mean slope steepness or curvature, respectively. Readouts are given as a function of the length of each of the four DGD sections forming the DGD profile “loop.” In the limit of small DGDs, the curvature differences are extremely small because they rise with the cube of the DGD per section. In contrast, the slope difference readout rises with the square of the DGD per section and is therefore for small DGDs much larger than the curvature difference readout. Unlike other detection criteria, the slope steepness difference is directly proportional to the DGD profile loop area. Surprisingly, the third-order effect QM (more precisely, PQM) is better detectable than the second-order effect LM. Yet, the slope difference measurement is fully sufficient because it detects the third-order PMD that is typically associated with second-order PMD. If input polarization and LM are parallel, the slope difference readout vanishes, but scrambling can ensure that this situation will not persist.

Let us look at alternative methods for detecting what occurs in Fig. 18. An auxiliary decision circuit with a variable threshold level, the output signal of which is compared to the output signal of the main decision circuit in an EXOR gate, indicates the inner eye opening. This measurement is digital. Being subject to corresponding strong quantization noise, it requires a long measurement interval to achieve an acceptable accuracy. In addition, the inner eye opening reduces with the third power of the DGD per section. The eye closure (= back-to-back eye opening minus actual inner eye opening), also plotted in Fig. 21, is therefore extremely small for small DGDs per section. Other than for the two aforementioned schemes, the eye-opening measurement is accompanied by the back-to-back eye opening as a large offset, which makes it difficult to reliably measure the smallest eye closures. In particular, the eye is also being closed by power loss, PDL, and patterning. Only a Q factor measurement can get around this, but an even longer measurement interval is needed.

Instead of adding, one could as well subtract the output signals of the oppositely poled rectifiers in the bottom of Fig. 20. This would result in a high-pass filter output power measurement because the differentiator is a high-pass filter. Maximizing this power by a suitable PMDC removes first-order PMD and also the curvature difference distortions that occur if the normalized Stokes vector of the input polarization and the plane of the DGD profile loop are perpendicular. However, that control strategy will try to enlarge any DGD profile loop that lies in a plane parallel to the input polarization, because the over-

shoot associated with the slope steepness differences actually increases the power of the detected signal. The high-pass filter output power also indicates the presence of the previously mentioned figure-eight DGD profile. Therefore, PMD compensation cannot work well if it is based on high-pass filter output power measurement alone. This control criterion tends to minimize first- and second-order PMD but maximize third-order PMD.

There is yet another point. High-pass filter output power measurement is strongly influenced by the bit pattern. Depending on how many signal transitions occur during a measurement interval, the readout may vary. For example, if there is a 101010 sequence instead of a pseudorandom binary sequence (PRBS), the readout increases. Curvature difference readouts are also sensitive to patterning. We tried a square-shaped DGD profile loop with four sections of length $0.1875T$ and found out that even the sign of the curvature difference was changed when we used a 110110110 sequence, instead of a PRBS. The explanation is that the 110110110 sequence avoids the single ones that have maximum negative curvature. In contrast, slope difference readouts are fairly little affected by patterning because there are always as many falling slopes as there are rising slopes—with an uncertainty of only one slope within any measurement interval.

Uncompensated fiber chromatic dispersion masks the slope steepness difference readout because it masks the corresponding PMD penalty. For ± 17 ps/nm, about half, and beyond ± 34 ps/nm essentially the whole slope steepness difference readout vanishes, at 40 Gb/s. While it is not difficult to stay within ± 17 ps/nm, one might wish to be able to tolerate somewhat more chromatic dispersion. On the other hand, if there is ± 34 ps/nm of uncompensated chromatic dispersion, the eye opening is reduced so much that accurate detection of higher order PMD is not important anyway.

The other previously mentioned higher order PMD detection schemes are cross-sensitive to chromatic dispersion, including its sign. If there is no scrambler, they can be helpful for compensation of fiber chromatic dispersion by a second-order PMD set to be parallel or antiparallel to the input polarization.

Table I summarizes, somewhat simplified, the pros and cons of the different methods suitable for detection of what occurs in Fig. 18. Slope steepness difference detection is an attractive candidate. It is straightforward to also measure the high-pass output power for inclusion into the control process, since no

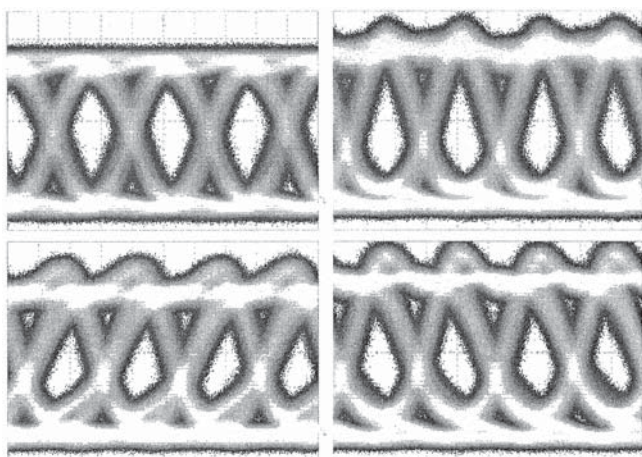


Fig. 22. 40 Gb/s eye diagrams (see text), comparable to those of Fig. 19.

more RF hardware is needed than for slope steepness difference detection.

The slope steepness difference can of course also be detected statically, without polarization scrambling, but not if this scheme is intended to indicate the presence of a DGD profile loop independent of its orientation.

When the distributed PMDC is set like shown in Fig. 16 at the optical carrier frequency, it allows the verification of the predicted higher order PMD effects. Fig. 22 shows corresponding measured 40 Gb/s eye diagrams. The top left is a back-to-back eye diagram. The other eye diagrams were obtained with the PMDC, for different fixed input polarizations. The top right depicts peaking due to maximum curvature difference. Eye shear in either direction was also obtained (bottom). These measurements confirm the simulations of Fig. 19.

VI. CONCLUSION

We have presented a “tennis ball” polarization scrambler with a single electrooptic waveplate for circular input polarization that generates only three harmonics of the Stokes’ parameters, and a polarization-independent polarization scrambler with two electrooptic waveplates. They can be used for arrival-time detection of PMD and for other PMD detection schemes that require a polarimeter. The PMD detection sensitivity for the tennis-ball scrambler in a 40 Gb/s NRZ transmission system was around 1 ps, using a 2.4 μ s measurement interval.

We have also implemented an inverse scattering algorithm for devices with PMD. It has enabled nondestructive determination of various differential group-delay profiles, in particular those of a distributed PMDC in X -cut, Y -propagation LiNbO_3 , which is capable of a number of mode conversions.

After compensation of first-order PMD, the DGD profile will typically consist of a loop or a similar closed trajectory. If there is a polarization scrambler at the transmitter, slope steepness differences will occur reliably. These can be detected by a differentiator with two subsequent, oppositely poled one-way rectifiers.

The combination of the discussed schemes and devices is expected to allow a cost-effective and powerful PMD compensation at 40 Gb/s.

ACKNOWLEDGMENT

The authors thank H. Herrmann, H. Suche, and W. Sohler (Applied Physics, University of Paderborn) for fabricating the distributed polarization-mode dispersion compensator. The clock and data recovery were provided by Infineon Technologies, and the voltage-controlled oscillator was provided by WORK Microwave GmbH. S. Chotchidjoun is acknowledged for having provided the analytical value of ϵ (Section II-B).

REFERENCES

- [1] R. Noé, “German Patent Application DE 100 50 266.0,” Oct. 9, 2000.
- [2] H. Rosenfeldt *et al.*, “Automatic PMD compensation at 40 Gbit/s and 80 Gbit/s using a 3-dimensional DOP evaluation for feedback,” presented at the OFC2001, Anaheim, CA, 2001, Postdeadline Paper PD27-1.
- [3] R. Noé, D. Sandel, V. Mirvoda, F. Wüst, and S. Hinz, “Polarization mode dispersion detected by arrival time measurement of polarization-scrambled light,” *J. Lightwave Technol.*, vol. 20, pp. 229–235, Feb. 2002.
- [4] H. Sunnerud, M. Westlund, J. Li, J. Hansryd, M. Karlsson, P.-O. Hedekvist, and P. A. Andrekson, “Long-term 160 Gb/s-TDM, RZ transmission with automatic PMD compensation and system monitoring using an optical sampling system,” presented at the ECOC 2001, Amsterdam, The Netherlands, Sept.–Oct. 30–4, 2001, Postdeadline Paper PD.M.1.9.
- [5] L.-S. Yan, Q. Yu, A. B. Sahin, Y. Wang, and A. E. Willner, “Simple bit-rate independent PMD monitoring for WDM systems,” presented at the ECOC 2001, vol. , Amsterdam, The Netherlands, Sept.–Oct. 30–4, 2001, Paper TU.A.3.2.
- [6] D. Sandel, F. Wüst, V. Mirvoda, and R. Noé, “Standard (NRZ 1×40 Gbit/s, 210 km) and polarization multiplex (CS-RZ, 2×40 Gbit/s, 212 km) transmissions with PMD compensation,” *IEEE Photon. Technol. Lett.*, vol. 14, pp. 1181–1183, Aug. 2002.
- [7] R. Noé, D. Sandel, S. Hinz, M. Yoshida-Dierolf, V. Mirvoda, G. Feise, H. Herrmann, R. Ricken, W. Sohler, F. Wehrmann, C. Glingener, A. Schöpflin, A. Färbert, and G. Fischer, “Integrated optical LiNbO_3 distributed polarization mode dispersion equalizer in 20 Gbit/s transmission system,” *Electron. Lett.*, vol. 35, no. 8, pp. 652–654, 1999.
- [8] L. Möller, “Filter synthesis for broad-band PMD compensation in WDM systems,” *IEEE Photon. Technol. Lett.*, vol. 12, pp. 1258–1260, Sept. 2000.
- [9] S. E. Harris, E. O. Ammann, and I. C. Chang, “Optical network synthesis using birefringent crystals—Part I. Synthesis of lossless networks of equal-length crystals,” *J. Opt. Soc. Amer.*, vol. 54, pp. 1267–1279, 1964.
- [10] R. Noé, “Combating and equalizing the effects of PMD in 40 Gb/s systems and beyond,” in *Proc. 28th Eur. Conf. Optical Communication (ECOC 2002)*, vol. II, Tutorial 4, Copenhagen, Denmark.
- [11] R. Noé, H. Heidrich, and D. Hoffman, “Endless polarization control systems for coherent optics,” *J. Lightwave Technol.*, vol. 6, pp. 1199–1207, July 1988.
- [12] V. Mirvoda, D. Sandel, F. Wüst, and R. Noé, “Optimized polarization scramblers for PMD detection,” in *Proc. 28th Eur. Conf. Optical Communication (ECOC 2002)*, vol. 3, Copenhagen, Denmark, 2002, p. 3.5.
- [13] B. L. Heffner, “Accurate, automated measurement of differential group delay dispersion and principal state variation using Jones matrix eigenanalysis,” *IEEE Photon. Technol. Lett.*, vol. 5, pp. 814–817, July 1993.
- [14] L. E. Nelson, R. M. Jopson, and H. Kogelnik, “Müller matrix method for determining polarization mode dispersion vectors,” in *Proc. ECOC 1999*, vol. II, Nice, France, Sept. 26–30, 1999, pp. 10–11.
- [15] G. J. Foschini, R. M. Jopson, L. E. Nelson, and H. Kogelnik, “Statistics of polarization dependent chromatic fiber dispersion due to PMD,” in *Proc. ECOC 1999*, vol. II, Nice, France, Sept. 26–30, 1999, pp. 56–59.
- [16] N. Kikuchi, “Adaptive chromatic dispersion compensation using higher order polarization-mode dispersion,” *IEEE Photon. Technol. Lett.*, vol. 13, pp. 1115–1117, Oct. 2001.
- [17] M. Amemiya, “Pulse broadening due to higher order dispersion and its transmission limit,” *J. Lightwave Technol.*, vol. 20, pp. 591–597, Apr. 2002.
- [18] G. J. Foschini and C. D. Poole, “Statistical theory of polarization dispersion in single-mode fibers,” *J. Lightwave Technol.*, vol. 9, pp. 1439–1456, Nov. 1991.

- [19] R. Noé, D. Sandel, M. Yoshida-Dierolf, S. Hinz, V. Mirvoda, A. Schöpflin, C. Glingener, E. Gottwald, C. Scheerer, G. Fischer, T. Weyrauch, and W. Haase, "Polarization mode dispersion compensation at 10, 20 and 40 Gb/s with various optical equalizers," *J. Lightwave Technol.*, vol. 17, pp. 1602–1616, Sept. 1999.

D. Sandel, photograph and biography not available at the time of publication.

V. Mirvoda, photograph and biography not available at the time of publication.

S. Bhandare, photograph and biography not available at the time of publication.

F. Wüst, photograph and biography not available at the time of publication.

R. Noé (M'93) was born in Darmstadt, Germany, in 1960. He received the Dipl.Ing. and Dr.Ing. degrees in electrical engineering from the Technical University of Munich, Germany, in 1984 and 1987, respectively.

At that time, he realized the first endless polarization control systems. He then spent a postdoctoral year at Bellcore, Red Bank, NJ. In 1988, he joined Siemens Research Laboratories, Munich, Germany, to work on coherent optical systems. Since 1992, he has been the Chair of Optical Communication and High-Frequency Engineering at the University Paderborn, Paderborn, Germany. Most of his recent work is on PMD detection and compensation and on polarization division multiplex. He has authored or coauthored more than 100 publications. He is one of the editors of *Electrical Engineering*, and he is a frequent referee for *Electronics Letters* and IEEE publications.